

120°) is 2.52 kJ/mol, which is comparable with the energy of thermal noise. Table 1 also demonstrates the necessity of a small positive charge in addition to the dipole moment to form sheets. Without net charge the lowest energy state is the bottom-side orientation, preventing the formation of 2D monolayers (fig. S11).

Using the same modeling strategy, one can consider NPs with different numbers of corners truncated. NPs with zero or one truncated corners cannot form 2D monolayers due to the steric constraints between the untruncated corners of adjacent NPs. NPs with two truncated corners form chains instead of monolayers (fig. S12). Although 2D self-assembly was observed only for NPs with three truncated corners, we do not exclude the existence of NPs with other number of truncated corners in the experimentally obtained sheets, including those with four truncated corners, because the net dipole moment inside those NPs can be induced by other adjacent NPs (24). The inclusions will show up as defects within the sheet (Fig. 1C). Nevertheless, the arrangement of NPs with three adjacent NPs in a 2D film is the most energetically favorable.

The interactions between NPs in general are complex and diverse, which offers tremendous opportunities for the design of NP assemblies with varying shapes, structures, and functions (31, 34). This study of 2D self-assembly of NPs demonstrates (i) the importance of anisotropy of interparticle interactions at the nanoscale and (ii) methods for the manipulation and prediction of spontaneous NP assemblies. These data also show

a surprising resemblance of NPs to self-ordering biological systems, such as S-layer-forming proteins (4–6). This is particularly important for establishing correlations between protein superstructures and inorganic nanostructures on the basis of their similar sizes.

References and Notes

1. A. P. Alivisatos, *Science* **271**, 933 (1996).
2. C. B. Murray, C. R. Kagan, M. G. Bawendi, *Annu. Rev. Mater. Sci.* **30**, 545 (2000).
3. Z. Y. Tang, N. A. Kotov, *Adv. Mater.* **17**, 951 (2005).
4. U. B. Sleytr, E. M. Egelseer, D. Pum, B. Schuster, in *Nanobiotechnology: Concepts, Applications, and Perspectives*, C. M. Niemeyer, C. A. Mirkin, Eds. (Wiley-VCH, Weinheim, Germany, 2004), pp. 77–92.
5. K. Jagannathan, R. W. Chang, A. Yethiraj, *Biophys. J.* **83**, 1902 (2002).
6. R. Flachmann, W. Kuhlbrandt, *Proc. Natl. Acad. Sci. U.S.A.* **93**, 14966 (1996).
7. Z. Tang, N. A. Kotov, M. Giersig, *Science* **297**, 237 (2002).
8. J. F. Banfield, S. A. Welch, H. Z. Zhang, T. T. Ebert, R. L. Penn, *Science* **289**, 751 (2000).
9. C. Pacholski, A. Kornowski, H. Weller, *Angew. Chem. Int. Ed.* **41**, 1188 (2002).
10. C. B. Murray, C. R. Kagan, M. G. Bawendi, *Science* **270**, 1335 (1995).
11. M. P. Pileni, *J. Phys. Chem. B* **105**, 3358 (2001).
12. A. L. Rogach *et al.*, *Adv. Funct. Mater.* **12**, 653 (2002).
13. C. Burda, X. B. Chen, R. Narayanan, M. A. El Sayed, *Chem. Rev.* **105**, 1025 (2005).
14. E. V. Shevchenko, D. V. Talapin, N. A. Kotov, S. O'Brien, C. B. Murray, *Nature* **439**, 55 (2006).
15. V. L. Colvin, A. N. Goldstein, A. P. Alivisatos, *J. Am. Chem. Soc.* **114**, 5221 (1992).
16. C. P. Collier, R. J. Saykally, J. J. Shiang, S. E. Henrichs, J. R. Heath, *Science* **277**, 1978 (1997).
17. Y. Lin, H. Skaff, T. Emrick, A. D. Dinsmore, T. P. Russell, *Science* **299**, 226 (2003).
18. A. L. Rogach *et al.*, *Ber. Bunsenges. Phys. Chem* **100**, 1772 (1996).
19. N. Gaponik *et al.*, *J. Phys. Chem. B* **106**, 7177 (2002).
20. C. R. Kagan, C. B. Murray, M. Nirmal, M. G. Bawendi, *Phys. Rev. Lett.* **76**, 1517 (1996).
21. S. A. Crooker, J. A. Hollingsworth, S. Tretiak, V. I. Klimov, *Phys. Rev. Lett.* **89**, 186802 (2002).
22. M. Shim, P. Guyot-Sionnest, *J. Chem. Phys.* **111**, 6955 (1999).
23. J. L. Gavartin, A. M. Stoneham, *Philos. Trans. R. Soc. London. A* **361**, 275 (2003).
24. K. S. Cho, D. V. Talapin, W. Gaschler, C. B. Murray, *J. Am. Chem. Soc.* **127**, 7140 (2005).
25. J. Polleux, N. Pinna, M. Antonietti, M. Niederberger, *Adv. Mater.* **16**, 436 (2004).
26. S. G. Thoma, A. Sanchez, P. P. Provencio, B. L. Abrams, J. P. Wilcoxon, *J. Am. Chem. Soc.* **127**, 7611 (2005).
27. A. A. Yaroslavov *et al.*, *J. Am. Chem. Soc.* **127**, 7322 (2005).
28. J. N. Israelachvili, *Intermolecular and Surface Forces: With Applications to Colloidal and Biological Systems* (Academic Press, New York, 1985), p. 296.
29. S. Shanbhag, N. A. Kotov, *J. Phys. Chem. B* **110**, 12211 (2006).
30. Z. L. Wang, *J. Phys. Chem. B* **104**, 1153 (2000).
31. Z. L. Zhang, S. C. Glotzer, *Nano Lett.* **4**, 1407 (2004).
32. M. S. Wertheim, *J. Stat. Phys.* **35**, 19 (1984).
33. G. D. Phillips, *J. Chem. Phys.* **60**, 2721 (1974).
34. Z. L. Zhang, M. A. Horsch, M. H. Lamm, S. C. Glotzer, *Nano Lett.* **3**, 1341 (2003).
35. Experiments were performed by Z.T. and Y.W. Simulations were performed by Z.Z. We thank the NSF (N.A.K.), U.S. Department of Energy (S.C.G.), Air Force Office of Scientific Research (N.A.K.), and Defense Advanced Research Projects Agency (N.A.K.) for the financial support of this research. Seed funding provided by the University of Michigan College of Engineering Nanotechnology Initiative is greatly appreciated. Z.Z. and S.C.G. thank C. Iacovella in the Glotzer group for graphics support. Z.T. and N.A.K. thank Z. L. Wang (Georgia Tech) for preliminary TEM observations.

Supporting Online Material

www.sciencemag.org/cgi/content/full/314/5797/274/DC1
Materials and Methods
Figs. S1 to S12

29 March 2006; accepted 29 August 2006
10.1126/science.1128045

Dynamic Stark Control of Photochemical Processes

Benjamin J. Sussman,^{1,2} Dave Townsend,¹ Misha Yu. Ivanov,¹ Albert Stolow^{1,2*}

A method is presented for controlling the outcome of photochemical reactions by using the dynamic Stark effect due to a strong, nonresonant infrared field. The application of a precisely timed infrared laser pulse reversibly modifies potential energy barriers during a chemical reaction without inducing any real electronic transitions. Dynamic Stark control (DSC) is experimentally demonstrated for a nonadiabatic photochemical reaction, showing substantial modification of reaction channel probabilities in the dissociation of IBr. The DSC process is nonperturbative and insensitive to laser frequency and affects all polarizable molecules, suggesting broad applicability.

Molecular catalysts increase chemical reaction rates by applying forces that modify potential energy barriers along a reaction coordinate. Because electrical forces underlie all of chemistry, such barrier manipulation is also possible by application of a laser

field. The duration of modern ultrafast laser pulses is on the time scale of chemistry itself, and therefore precise control over the form and delay of these pulses offers access to different portions of a potential energy surface as a reaction occurs. DSC is a technique that uses nonresonant infrared laser fields to dynamically alter a potential energy landscape during a photochemical reaction. The application of this field modifies the potential surface via the Stark effect, enhancing or inhibiting a specific reaction channel. Importantly, it does so without inducing

any real electronic transitions to other potential surfaces, which can lead to chemical reactions other than the one of interest. DSC will be general because the nonresonant Stark effect is independent of the laser frequency and is applicable to all quantum systems.

The control of chemical reactions by lasers is an area of great interest (1–3). Quantum control can be viewed as chemistry where light is used as a photonic reagent (4). By contrast, we experimentally demonstrated that the nonresonant dynamic Stark effect participates in quantum control by altering reaction barriers, as if it were a photonic catalyst. Because all strong-field approaches tacitly contain the dynamic Stark effect, DSC can be considered as a fundamental element of the quantum control toolbox (5). However, by exclusively utilizing the dynamic Stark effect, DSC avoids the ionizing fields that can produce numerous competing processes, such as Coulomb explosion (6), enhanced ionization (7), and nonadiabatic multi-electron ionization (8). Perturbative coherent control approaches do not modify potential energy surfaces but rather use interference between two or more real electric dipole transitions (I). Strong dipole coupling of states in nonper-

¹Steele Institute for Molecular Sciences, National Research Council of Canada, 100 Sussex Drive, Ottawa, Ontario K1A 0R6, Canada. ²Department of Physics, Queen's University, Kingston, Ontario K7L 3N6, Canada.

*To whom correspondence should be addressed. E-mail: albert.stolow@nrc.ca

turbative laser fields creates light-induced potentials that lead to phenomena such as static and transient bond hardening or softening (3, 9). Optical pulses shaped by feedback-learning algorithms (10) can optimize, via multiphoton transitions, the yield of a chosen product, as demonstrated in the strong-field ionization-fragmentation of polyatomic molecules (11, 12). Theoretical studies of laser catalysis (via electronic transitions) of ground-state collision processes investigated the line shape for the reaction probability as a function of optical frequency (13, 14) or, alternatively, considered resonantly induced couplings during the collision (15). Moving wave packets between potential energy surfaces can likewise be used to avoid ground-state barriers (2).

Fig. 1. DSC of IBr dissociation. An excited state wavepacket traversed a nonadiabatic crossing, correlating to either $\text{Br}(^2P_{3/2})$ or $\text{Br}^*(^2P_{1/2})$ products. As the bond was breaking, an ultrafast IR field was used to dynamically modify the adiabatic potential barrier (inset) via the Stark effect, mediating the reaction outcome. Because no transitions to other electronic states were involved, the system always remained on these two coupled potentials.

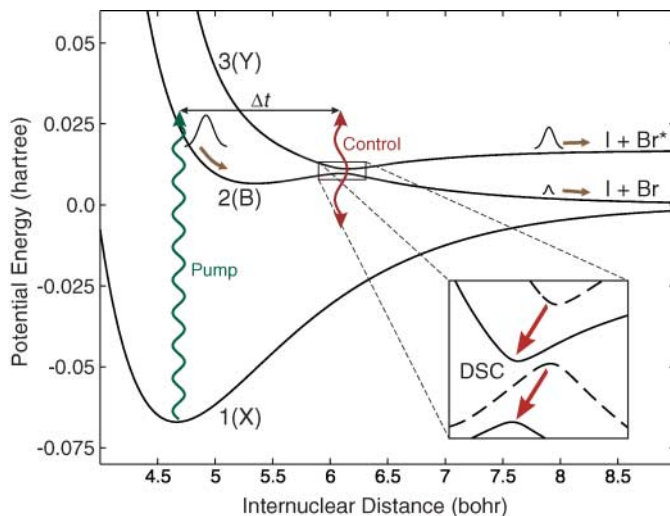
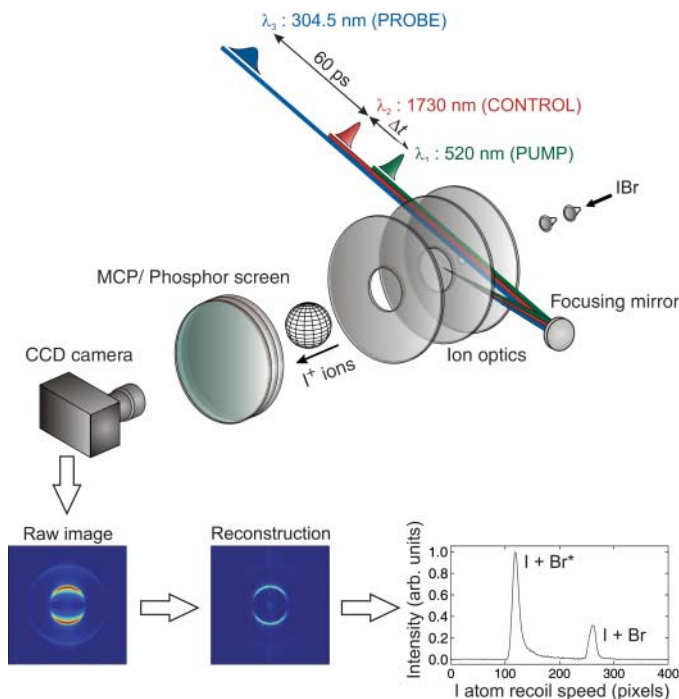


Fig. 2. Experimental demonstration of DSC of IBr dissociation. Dissociation of jet-cooled IBr was initiated with a 520-nm fs pulse. A delayed 1.7- μm fs control pulse was applied, modifying the reaction barrier and leading to a change in the chemical branching ratio. Long after dissociation, free neutral ground-state iodine atom products were ionized with a narrow band 304.5-nm laser. The recoiling ions were dispersed through the ion optics of a VMI spectrometer and imaged by a detector, and their velocity distributions were reconstructed. The iodine recoil velocity distribution directly reveals the Br^*/Br branching ratio. The inner ring of the image corresponds to $\text{I}+\text{Br}^*$, whereas the outer corresponds to $\text{I}+\text{Br}$ production.



To demonstrate DSC, we applied it to an important class of photochemical reactions: non-adiabatic processes. These processes, such as internal conversion or intersystem crossing, entail charge rearrangements that occur along a reaction path at the intersections of potential energy surfaces and act as triggers of the ensuing chemistry. Nonadiabatic processes are of paramount importance in the biological mechanisms of vision and photosynthesis and underlie the photochemistry of almost all polyatomic molecules (16). Chemical branching ratios in non-adiabatic processes are very sensitive to the intersection geometry, and therefore the dynamic modification of these processes is an important application of DSC. We specifically applied DSC to the canonical example of a nonadiabatic

process, photodissociation of IBr (17–19). The reaction is initiated by absorption of a visible photon, making the transition from the ground state $1(X)$ to $2(B)$ (Fig. 1). The non-adiabatic intersection between states $2(B)$ and $3(Y)$ leads to two chemically distinct, neutral atomic channels: $\text{IBr} \rightarrow \text{I} + \text{Br}(^2P_{3/2})$ and $\text{I} + \text{Br}^*(^2P_{1/2})$. These Br and Br^* atomic products have different chemical reactivity and play an important role in the destruction of ozone (20), especially in the marine boundary layer (21). An infrared DSC field was used to modify the curve-crossing barrier at a specific time, thus promoting the yield of one chosen product over another.

DSC of IBr photodissociation was demonstrated by using a molecular beam technique. Briefly described, a seeded supersonic jet of IBr in argon was produced by expansion through a 200- μm -diameter glass capillary nozzle (Fig. 2). Glass and polytetrafluoroethylene parts were used exclusively to avoid the decomposition of IBr. The reaction was initiated by a 100-fs laser pulse centered at 520 nm, above the dissociation limit for both channels. To achieve DSC, we focused a time-delayed 1.7- μm infrared pulse, 150 fs in duration, to nonperturbative intensities (22). To maximize the effects of DSC, we set the laser intensity to just below the threshold for ionization (i.e., below 10^{13} W/cm^2).

Importantly, a third weak laser field was used as the final probe of free neutral product formation. About 60 ps after the pump and catalysis pulses, free neutral ground-state iodine atoms produced in the reaction were selectively detected via (2+1) resonance-enhanced multiphoton ionization (REMPI) by using a 304.5-nm pulse of 0.4-nm linewidth. Conservation of energy and momentum dictate that the iodine fragments from the Br^* channel have a lower velocity than those from the Br channel. Therefore, measurement of the iodine atom kinetic energy distribution permits unambiguous determination of the Br^*/Br product branching ratio. This approach avoids uncertainties in the relative ionization cross sections of the chemically distinct Br and Br^* . The velocity distribution of the iodine fragments was measured by using velocity map imaging (VMI), a charged-particle spectrometry technique that maps velocity to position, permitting the measurement of three-dimensional fragment velocity distributions (23).

A typical fourfold symmetrized velocity-mapped image was obtained under control-free conditions (i.e., 520-nm initiation and 304.5-nm I-atom probe beams only) and is presented along with its associated Abel inverted reconstruction and speed distribution (Fig. 2). The field-free branching ratio is $\text{Br}^*/\text{Br} = 3.5$, in good agreement with previous measurements (24). Changes in the branching ratio due to the application of the infrared (IR) control field are easily and accurately determined from the VMI reconstructed speed distribution.

The mechanism underlying DSC's ability to reshape the potential energy barriers is the

nonresonant dynamic (or AC) Stark effect (25). This effect is similar to the well-known static (or DC) Stark effect but with several important distinctions. Infrared laser frequencies in the nonresonant 1.5- to 2- μm region are large with respect to rotational and vibrational frequencies but small with respect to electronic transition frequencies, and, hence, no single photon transitions can occur. In this situation, the dynamic Stark effect can be insensitive to the laser frequency, following instead the intensity envelope of the pulse (26). This property produces a quasi-static energy-level shift that reversibly follows the envelope of the laser pulse, avoiding all real electronic transitions (including ionization). The reaction Hamiltonian returns to its field-free form after the DSC pulse has passed, and, in this sense, DSC modifies the propagator during the propagation. Ultrafast lasers can produce vastly higher fields and more rapidly varying intensity envelopes than can DC

electric field sources; therefore, they have the capacity to strongly shape a specific potential energy landscape on ultrafast time scales.

State intersection problems can be considered in two representations, the diabatic and the adiabatic, which are connected by a unitary transformation. In the limit of slow velocity along the reaction coordinate, the system follows the adiabatic potential. In the limit of high velocity, it follows the diabatic potential. The Landau-Zener (LZ) formalism offers insight into how DSC affects the curve-crossing probability (27). The simple LZ formula gives the probability for nonadiabatically hopping from one surface to another: $P = \exp\{-2\pi V_{23}^2/v\partial_R[V_2(R) - V_3(R)]\}$, where R is the reaction coordinate, v is the reaction coordinate velocity, V_{23} is the coupling between the channels, and the V_i terms are the diabatic potential energy surfaces. In IB, the two diabatic curves correlate to atomic states that are not dipole coupled, and estimates

suggest that the dipole coupling between these diabats is small compared with all other couplings (28). The parameters on which P depends are all influenced by the dynamic Stark effect. A key effect is the differential Stark shifting of the diabatic potential energy surfaces, which displaces the crossing point so that the coordinate velocity at the intersection is altered. DSC can also be understood in terms of the adiabatic potentials as $A_{2,3} = \frac{1}{2}(V_2 + V_3) \pm \frac{1}{2}\sqrt{(V_2 - V_3)^2 + 4V_{23}^2}$. The adiabatic potential barriers rise and fall as the diabats are Stark shifted, altering the wavepacket velocity and hence the hopping probability. Therefore, the simple LZ formula suggests that one can expect sensitive catalytic control by altering the barrier at the intersection.

The raw I-atom speed distributions were plotted as a function of control pulse delay, Δt (Fig. 3). A key point is that at all delay times the recoil velocities of the I atom fragments remain essentially constant (i.e., follow vertical lines), demonstrating that IR control field has not excited new electronic states. There are two time delays when the reaction is critically sensitive to the control field: during initiation and during traversal of the crossing point. If the applied control pulse is simultaneous with the initiation pulse, the reaction begins on a Stark-shifted surface. The Stark lowering of the ground state has an effect equivalent to spectrally red-shifting the initiation wavelength. The result is that, as the control pulse fades, the wavepacket velocity is transiently reduced at the crossing point, decreasing the hopping probability and enhancing the Br channel. Application of the control pulse during traversal shifts and lowers the adiabatic barrier, thereby increasing the Landau-Zener hopping probability and thus production of Br*. Alternatively, in the diabatic picture, the crossing point shifts in the field, leading to a modified velocity at that point.

DSC is demonstrated by the variation of the overall integrated Br*/Br branching ratio as a function of IR pulse delay, Δt (Fig. 4). At early and late times, the speed distribution is identical to that of the molecule under field-free conditions. This result demonstrates the truly reversible nature of the DSC interaction: There are no real electronic or ionizing transitions due to the application of the control pulse. Application of the control field at $\Delta t = 0$ fs results in a 60% enhancement of Br yield at the expense of the Br* channel. Conversely, during control at $\Delta t = 300$ fs (traversal of the crossing), the reaction favors Br* production by more than 30%. The peak-to-valley contrast is over 90%, and, importantly, control is exerted on 100% of the reacting population. The experimental result is compared with numerical simulations based on a three-state split-operator approach, described elsewhere (29). The maximal Stark shifts used in the simulations are +0.125 eV for the diabatic $Y^3\Sigma^-(O^+)$ state and -0.022 eV for the diabatic $B^3\Pi(O^+)$ state. The simulation results are in good agreement

Fig. 3. Experimental iodine velocity distributions showing the two exit channels as a function of control pulse time delay. At each time delay Δt , the distribution is measured as in Fig. 2. By changing the control pulse delay, the branching fraction at the non-adiabatic crossing can be drastically altered. The smaller radius (velocity) corresponds to Br*; the higher, to Br. At early and late delays, the field-free branching ratio is observed, demonstrating the reversible nature of the DSC interaction.

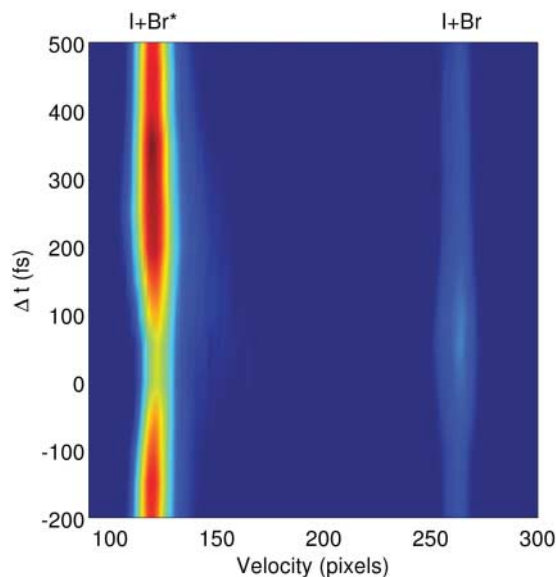
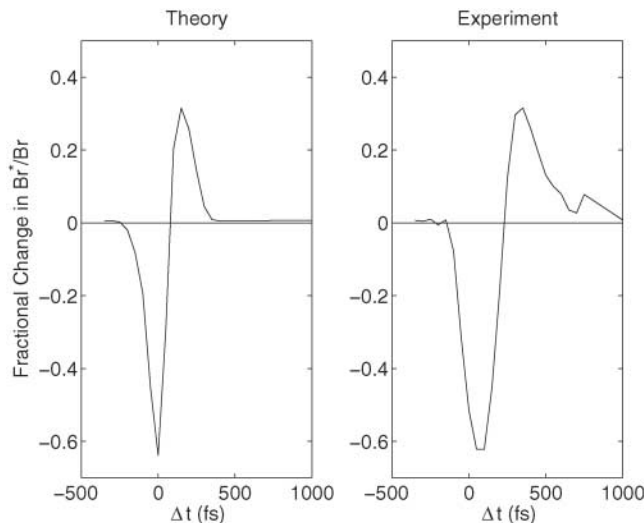


Fig. 4. Theoretical and experimental fractional changes in the branching ratio Br*/Br. The branching fraction is measured by taking the ratio of the integrated intensities of the two peaks in Fig. 3 as a function of Δt , the control pulse time delay.



with experiment, and although the polarizabilities of the (relativistic) IBr states are difficult to calculate (30), DSC will always be possible if there are differential polarizabilities between states.

We have shown that the nonresonant dynamic Stark effect can be used to dynamically alter a potential energy barrier in a photochemical reaction, promoting the formation of a given product. Variants of DSC that incorporate Raman pumping will be applicable to ground-state reactions. Pulse-shaping methods from the quantum control toolbox will also prove useful. For example, implementing DSC with adaptive-feedback techniques will lead to the design of custom-shaped Stark-control laser pulses. As well, it will be possible to use interference effects in DSC to alter, for example, excited-state lifetimes (29). The frequency independence, the avoidance of excited state chemistry, and the universal applicability of the nonresonant dynamic Stark effect should prove important for scaling DSC to larger and more complex systems.

References and Notes

1. P. W. Brumer, M. Shapiro, *Principles of the Quantum Control of Molecular Processes* (Wiley-Interscience, Hoboken, NJ), 2003).
2. S. A. Rice, M. Zhao, *Optical Control of Molecular Dynamics* (Wiley, New York, 2000).
3. A. D. Bandrauk, Ed., *Molecules in Laser Fields* (Marcel Dekker, New York, 1994).
4. H. Rabitz, *Science* **299**, 525 (2003).
5. H. Rabitz, R. de Vivie-Riedle, M. Motzkus, K. Kompa, *Science* **288**, 824 (2000).
6. L. J. Frasinski *et al.*, *Phys. Rev. Lett.* **58**, 2424 (1987).
7. C. Cornaggia, J. Lavancier, D. Normand, J. Morelle, H. X. Liu, *Phys. Rev. A* **42**, 5464 (1990).
8. M. Lezius *et al.*, *Phys. Rev. Lett.* **86**, 51 (2001).
9. H. Niikura, P. B. Corkum, D. M. Villeneuve, *Phys. Rev. Lett.* **90**, 203601 (2003).
10. R. S. Judson, H. Rabitz, *Phys. Rev. Lett.* **68**, 1500 (1992).
11. A. Assion *et al.*, *Science* **282**, 919 (1998).
12. R. J. Levis, G. M. Menkir, H. Rabitz, *Science* **292**, 709 (2001); published online 29 March 2001 (10.1126/science.1059133).
13. M. Shapiro, Y. Zeiri, *J. Chem. Phys.* **85**, 6449 (1986).
14. A. Vardi, M. Shapiro, *Phys. Rev. A* **58**, 1352 (1998).
15. T. F. George, J.-M. Yuan, I. H. Zimmerman, J. R. Laing, *Faraday Discuss. Chem. Soc.* **62**, 246 (1977).
16. W. Domcke, D. R. Yarkony, H. Koepfel, Eds., *Conical Intersections: Electronic Structure, Dynamics, and Spectroscopy* (World Scientific, Singapore, 2004).
17. M. Child, *Mol. Phys.* **32**, 1495 (1976).
18. C. K. Chan, P. Brumer, M. Shapiro, *J. Chem. Phys.* **94**, 2688 (1991).
19. P. Gross, D. B. Bairagi, M. K. Mishra, H. Rabitz, *Chem. Phys. Lett.* **223**, 263 (1994).
20. R. R. Garcia, S. Solomon, *J. Geophys. Res.* **99**, 12937 (1994).
21. R. Vogt, R. Sander, R. von Glasow, P. J. Crutzen, *J. Atmos. Chem.* **32**, 375 (1999).
22. The 1-kHz laser system consists of a Ti:Sapphire oscillator pumping a regenerative amplifier. The 800-nm output pumps a pair of optical parametric amplifiers (OPAs). The idler output from OPA1 (1730 nm) was used for the control pulse, whereas the signal (1485 nm) was mixed with residual 800-nm light to produce the 520-nm pump wavelength. The signal beam from OPA2 (1218 nm) was doubled and then doubled again to make the 304.5-nm ultraviolet (UV) probe. The REMPI probe is bandwidth-narrowed by use of long doubling crystals to ensure high selectivity. Telescopes were used to expand the three beams to varying diameters such that the focal-spot size ratios at the interaction region were UV:visible:IR = 1:1.5:2. Careful co-collimation then assured that the IR field was sampled at a uniform intensity.
23. A. T. J. B. Eppink, D. H. Parker, *Rev. Sci. Instrum.* **68**, 3477 (1997).
24. E. Wrede *et al.*, *J. Chem. Phys.* **114**, 2629 (2001).
25. B. W. Shore, *The Theory of Coherent Atomic Excitation*, vols. I and II (Wiley, New York, 1990).
26. B. J. Sussman, J. G. Underwood, R. Lausten, M. Y. Ivanov, A. Stolow, *Phys. Rev. A* **73**, 053403 (2006).
27. C. Y. Zhu, Y. Teranishi, H. Nakamura, *Adv. Chem. Phys.* **117**, 127 (2001).
28. M. Shapiro, H. Bony, *J. Chem. Phys.* **83**, 1588 (1985).
29. B. J. Sussman, M. Y. Ivanov, A. Stolow, *Phys. Rev. A* **71**, 051401 (2005).
30. S. Patchkovskii, *Phys. Chem. Chem. Phys.* **8**, 926 (2006).
31. We thank P. Corkum and M. Shapiro for many useful discussions and R. Lausten, R. Bhardwaj, and D. Rayner for their assistance with the experiment.

10 July 2006; accepted 23 August 2006
10.1126/science.1132289

Coherent Dynamics of Coupled Electron and Nuclear Spin Qubits in Diamond

L. Childress,^{1*} M. V. Gurudev Dutt,^{1*} J. M. Taylor,¹ A. S. Zibrov,¹ F. Jelezko,² J. Wrachtrup,² P. R. Hemmer,³ M. D. Lukin^{1†}

Understanding and controlling the complex environment of solid-state quantum bits is a central challenge in spintronics and quantum information science. Coherent manipulation of an individual electron spin associated with a nitrogen-vacancy center in diamond was used to gain insight into its local environment. We show that this environment is effectively separated into a set of individual proximal ¹³C nuclear spins, which are coupled coherently to the electron spin, and the remainder of the ¹³C nuclear spins, which cause the loss of coherence. The proximal nuclear spins can be addressed and coupled individually because of quantum back-action from the electron, which modifies their energy levels and magnetic moments, effectively distinguishing them from the rest of the nuclei. These results open the door to coherent manipulation of individual isolated nuclear spins in a solid-state environment even at room temperature.

The controlled, coherent manipulation of quantum-mechanical systems is an important challenge in modern science and engineering (1). Solid-state quantum systems such as electronic spins (2–10), nuclear spins (11, 12), and superconducting islands (13) are among the most promising candidates for re-

alization of qubits. However, in contrast to isolated atomic systems (14), these solid-state qubits couple to a complex environment, which often leads to rapid loss of coherence and, in general, is difficult to understand (15–19).

We used spin-echo spectroscopy on a single-electron solid-state qubit to gain insight into its local environment. We investigated a single nitrogen-vacancy (NV) center in a high-purity diamond sample and showed that its electron spin coherence properties are determined by ¹³C nuclear spins. Most importantly, we demonstrated that the electron spin couples coherently to individual proximal ¹³C spins. By selecting an NV center with a desired nearby ¹³C nucleus and adjusting the external magnetic

field, we could effectively control the coupled electron-nuclear spin system. Our results show that it is possible to coherently address individual isolated nuclei in the solid state and manipulate them via a nearby electron spin. Because of the long coherence times of isolated nuclear spins (20), this is an important element of many solid-state quantum information approaches from quantum computing (11, 12) to quantum repeaters (21, 22).

Spin echo is widely used in bulk electron spin resonance (ESR) experiments to study interactions and to determine the structure of complex molecules (23). Recently, local contact interactions were observed between single-NV electronic spins and the nuclear spins associated with the host nitrogen and the nearest-neighbor carbon atoms (3, 24). In the latter case, coherent dynamics of electron and nuclear spins were observed (3). We show that coherent coupling extends to separated isolated nuclei, which nominally constitute the electron environment and couple weakly to the electron spin.

The NV center stands out among solid-state systems because its electronic spin can be efficiently prepared, manipulated, and measured with optical and microwave excitation (2). The electronic ground state of the NV center is a spin triplet that exhibits a 2.87-GHz zero-field splitting, defining the \hat{z} axis of the electron spin (Fig. 1A). Application of a small magnetic field splits the magnetic sublevels $m_s = \pm 1$, allowing selective microwave excitation of a single spin transition.

Our observations can be understood by considering how the NV electron spin interacts

¹Department of Physics and Institute for Quantum Science and Engineering, Harvard University, Cambridge, MA 02138, USA.

²Physikalisches Institut, Universität Stuttgart, Pfaffenwaldring 57 D-70550 Stuttgart, Germany. ³Department of Electrical and Computer Engineering, Texas A&M University, College Station, TX 77843, USA.

*These authors contributed equally to this work.

†To whom correspondence should be addressed. E-mail: lukin@fas.harvard.edu